PHOTONICS Research

On-chip sorting of orbital angular momentum beams using Bloch surface wave structures

NANNAN LI,[1,†] QI ZOU,[1,†] YIZHI LAN,[1] YAQI WANG,[1] JUN ZHANG,[1] MICHAEL SOMEKH,[1,2,3,4]
CHANGJUN MIN,[1,5] FU FENG,[1,2,6] AND XIAOCONG YUAN[1,2,7]

[1]*Nanophotonics Research Center, Institute of Microscale Optoelectronics & State Key Laboratory of Radio Frequency Heterogeneous Integration, Shenzhen University, Shenzhen 518060, China*
[2]*Research Center for Humanoid Sensing, Zhejiang Lab, Hangzhou 311100, China*
[3]*Faculty of Engineering, University of Nottingham, Nottingham NG7 2RD, UK*
[4]*e-mail: michael.somekh@nottingham.ac.uk*
[5]*e-mail: cjmin@szu.edu.cn*
[6]*e-mail: fufeng@zhejianglab.com*
[7]*e-mail: xcyuan@szu.edu.cn*
[†]*These authors contributed equally to this work.*

Owing to their unique optical properties and new degrees of freedom, orbital angular momentum (OAM) beams have been applied in various fields. Detection of the topological charges (TCs) of OAM beams is the key step for their applications. However, on-chip sorting of OAM beams with large TCs still remains a challenge. In this paper, Bloch surface wave (BSW) structures with five semi-ring shaped nanoslits are modeled. A spatial separation of 135 nm on the chip is obtained between two neighboring OAM states. OAM beams with TCs up to 35 can be successfully sorted by the BSW structures, which is much larger than that using metallic structures (only seven). BSW structures exhibit better OAM sorting performances than metallic structures. We systematically show how the lower attenuation of BSW structures leads to far superior separation ability compared to surface plasmons propagating on metallic structures. In addition, sorting of two OAM beams with different TCs simultaneously can be achieved in this way. Our results reveal that BSW structures should be an excellent solution for OAM sorting with large TCs, which is beneficial for applications in integrated on-chip devices and optical communications. © 2023 Chinese Laser Press

https://doi.org/10.1364/PRJ.502760

1. INTRODUCTION

Orbital angular momentum (OAM) beams possess a helical phase wavefront and carry OAM information [1–4]. There is a phase singularity at the center of OAM beams, giving rise to a hollow intensity distribution. The azimuthal variation of the electric field profiles of OAM beams can be expressed as $\exp(il\varphi)$, where l and φ are the topological charge (TC) and the azimuthal angle, respectively [4]. TC is a crucial characteristic for OAM beams. OAM beams with different TCs are orthogonal to each other [5,6]. The orthogonal property makes it possible to use multiple OAM beams as signal channels to carry information in free space without crosstalk, which is beneficial for high-capacity data transmission and optical communication [7–11]. In addition, owing to their unique optical properties and new degrees of freedom, OAM beams have been applied in various fields, including optical tweezers [12–14], quantum entanglement [15–17], nonlinear optics [18–20],

nanofabrication and optical machining [21–23], high-resolution imaging [24–26], chemical and bio-molecule detection [27–29], and astronomy [30–32].

Detection of the TCs of OAM beams, namely, OAM sorting, is a key means to investigate their properties. Sorting of OAM beams also exhibits technological importance. The traditional strategies of OAM sorting usually employ spatial light modulators (SLMs) or other phase masks to carry out phase transformation and reconstruct the target phase. These strategies include fork diffraction gratings [33–36], liquid crystal q-plates [37–39], Faraday rotation interferometric devices [40], and optical geometric transformation [41–43]. Nevertheless, these traditional strategies require complex and bulky equipment, and the target beams need to be aligned accurately with the equipment. These drawbacks limit their applications. Recently, on-chip detection of OAM beams has emerged rapidly [44], since the detection chips can be highly compact,

portable, and easy to integrate with other devices [45]. The previous reports describing on-chip sorting of OAM beams all employ metallic structures [46–49]. However, surface plasmon polaritons (SPPs) using metallic structures usually suffer from severe Ohmic loss. The propagation length of SPPs is small, and this attenuation brings severe constraints in the geometry of the resulting structure. As a result, on-chip sorting of OAM beams with large TCs still remains a challenge.

On the other hand, Bloch surface waves (BSWs) are surface electromagnetic waves that appear at the interface between a periodic multilayer of dielectric materials and the surrounding medium, which are considered as the dielectric analogue of SPPs [50,51]. BSWs can be excited under the incident light with both transverse electric (TE) and transverse magnetic (TM) polarizations [51,52]. Since BSW structures consist of a periodic multilayer of dielectric materials, absorption loss of BSWs is much lower in comparison with that of SPPs [50–52]. The low-loss property endows BSWs with longer propagation lengths and sharper resonance peaks, and BSW structures have been widely applied in high-sensitivity sensing [51–54], high-contrast imaging [55], metallic particle trapping [56], and diffraction-free waveguides [57–59]. BSW structures therefore provide a promising solution for on-chip sorting of OAM beams with large TCs, which has not been explored before.

In this paper, we numerically investigate the on-chip sorting of OAM beams using BSW structures. The designed BSW structures consist of three dielectric layers, and five semi-ring shaped nanoslits were introduced on the top surface of the BSW structures. BSWs can be excited and modulated by the helical phase wavefront of the incident OAM beams. There is a transverse shift for the focal point owing to the constructive interference of the BSW. A spatial interval of 135 nm on the chip between two neighboring OAM states can be obtained by using BSW structures. Furthermore, OAM sorting behavior of metallic structures with the same morphology is also analyzed. OAM beams with TCs up to 35 can be successfully sorted by the BSW structures, which is much larger than that using metallic structures (only seven). BSW structures exhibit superior OAM sorting performances than SPPs due to the lower attenuation, which is beneficial for OAM sorting with large TCs. In addition, sorting of two OAM beams with different TCs simultaneously can be achieved in this way as long as the difference between these two TCs is no less than four. To our knowledge, this is the first demonstration of on-chip sorting of OAM beams with TCs up to 35 as well as the first report of on-chip sorting of two OAM beams simultaneously. Our results reveal that BSW structures could be an excellent solution for OAM sorting with large TCs, which is beneficial for applications in integrated on-chip devices and optical communication.

2. PRINCIPLE AND MODELING

The designed structure for exciting BSWs is schematically sketched in Fig. 1(a). The designed BSW structure consists of three layers, which are Si (top), SiO$_2$ (middle), and Si substrate (bottom). The refractive indexes of Si and SiO$_2$ were set as $n_h = 3.48 + 0.001i$ and $n_l = 1.47 + 0.005i$ [52], respectively. The thicknesses of the top Si layer and SiO$_2$ layer were

set as $d_h = 0.12\ \mu m$ and $d_l = 1.88\ \mu m$, respectively. This structure was illuminated by incident light from the bottom. Finite element methods were employed to numerically calculate the absorption and electric field distribution of this structure. Boundary conditions with perfectly matched layers were utilized on all sides in the simulations. Under incident light with TE polarization, the dispersion relation of the BSW structure described by absorption as a function of incidence angle is shown in Fig. 1(b). The white dashed line indicates the wavelength of 1.55 μm, which is chosen as the working wavelength in this study. The absorption spectrum of the structure as a function of incidence angle at 1.55 μm under TE polarization is also plotted [top subfigure in Fig. 1(b)]. It can be observed that the absorption reaches a maximum value of 0.985 at 24.98° at 1.55 μm. Figure 1(c) shows the electric field distribution of this structure under an incidence angle of 24.98° at 1.55 μm under TE polarization. The electric field reaches maximum at the top surface of the structure and decays gradually in air. The real part of the refractive index of the structure is also plotted for comparison [top subfigure in Fig. 1(c)]. These results show that BSWs are successfully excited on the top surface of this structure.

In order to perform on-chip sorting of OAM beams, several semi-ring shaped nanoslits were introduced on the top surface of the BSW structure. The mechanism of the OAM sorting methods is schematically illustrated in Fig. 1(d). We first consider the case of only one nanoslit. Considering the circularly polarized incident light with a phase profile of $\exp(il\varphi)$, the electric field at the surface can be expressed as [46]

$$E(r,\varphi) = \int_0^\pi |\vec{r}_0 - \vec{r}|^{-\frac{1}{2}} \exp[i(l+s)\varphi] \exp(ik_{BSW}|\vec{r}_0 - \vec{r}|)d\varphi, \tag{1}$$

where $\vec{r}$ is the position vector of the observing point P. $\vec{r}_0$ is the position vector of an arbitrary point on the semi-ring nanoslit. l denotes the TC of the incident OAM beams. s refers to the spin angular momentum (SAM) of the circularly polarized incident light. φ is the azimuthal angle. k_{BSW} refers to the wavevector of the BSW. Due to the helical phase of the OAM beams, the phase along the semi-ring nanoslit has a linear dependence on the azimuthal angle φ. In this case, the excited BSWs do not focus at the original point O, and there is a transverse shift for the focal region. The details of the derivation of Eq. (1) are introduced in Appendix A. The transverse peak position of the focal point can be derived as

$$x_j = \text{sgn}(j)\frac{\mu_j}{2\pi}\lambda_{BSW}, \tag{2}$$

where $j = l + s$, and j is the total angular momentum. μ_j is the first non-zero coefficient of $J'_j(x)$ [the derivative of $J_j(x)$]. λ_{BSW} is the effective wavelength of BSW. According to Eq. (2), the transverse peak position of the focal point is only determined by j and λ_{BSW}. s equals one for right-handed circular polarization (RCP), while s equals –1 for left-handed circular polarization (LCP). For multiple semi-ring nanoslits with different radii, the transverse position of the focal point remains the same since Eq. (2) is independent of the radius of the nanoslit. In addition, the above analysis of OAM sorting mechanism is also valid for
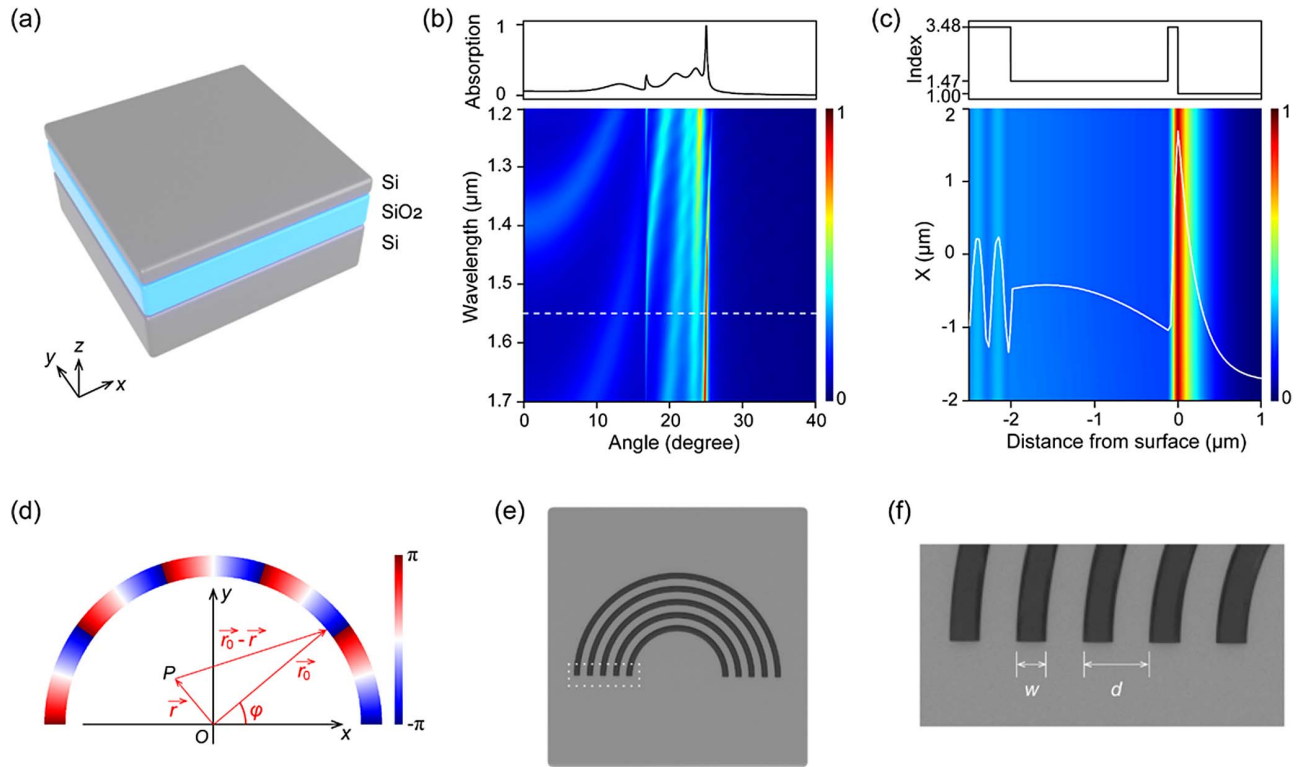
Fig. 1. Designed structure for exciting BSWs. (a) Schematic of the structure composed of three layers: Si (top), SiO$_2$ (middle), and Si substrate (bottom). (b) Dispersion relation of the structure described by absorption as a function of incidence angle under TE polarization. The white dashed line indicates the wavelength of 1.55 μm. The absorption spectrum of the structure as a function of incidence angle at 1.55 μm is plotted in the top subfigure. (c) Electric field distribution of the structure at incidence angle of 24.98° at 1.55 μm under TE polarization. The white curve refers to the electric field. The real part of the refractive index of the structure is plotted in the top subfigure. (d) Schematic of the mechanism of the OAM sorting methods. Only one nanoslit is considered. The phase along the semi-ring nanoslit has a linear dependence on the azimuthal angle φ. (e) Schematic of the designed BSW structure with five semi-ring shaped nanoslits. (f) Schematic of the geometric parameters of the BSW structure.

radially polarized and linearly polarized incident light (see Appendix A).

The designed structure for OAM sorting is schematically sketched in Fig. 1(e). The number of the nanoslits was chosen as five (as explained in the following section). The geometric parameters of the BSW structure are schematically shown in Fig. 1(f). The width of the nanoslits w was set as 0.6 μm, and the depth of the nanoslits was set as 0.2 μm. The geometry of the nanoslits was optimized to make the electric field at the focal point as large as possible. The period of the nanoslits s (the radial distance between two neighboring slits) was set to be λ_{BSW} to enhance the electric field intensity at the focal point. λ_{BSW} can be calculated as [52]

$$\lambda_{\mathrm{BSW}} = \frac{\lambda_0}{n_{\mathrm{eff}}} = \frac{\lambda_0}{n \sin \theta}, \qquad (3)$$

where λ_0 is the wavelength of the incident light (1.55 μm), n_{eff} is the effective refractive index, n is the refractive index of the Si substrate (3.48), and θ is the incidence angle where BSW is excited (24.98°). λ_{BSW} is calculated to be 1.054 μm. In this study, the period of the nanoslits d was set as 1.05 μm. The excitation angle of the TM mode of this dielectric structure is different from that of TE mode, so the effective wavelength of the TM mode is different. The five nanoslits with a period of

1.05 μm can serve as optical gratings, which selectively excite TE mode.

3. RESULTS AND DISCUSSION

A schematic of the designed BSW structure with five semi-ring shaped nanoslits is shown in Fig. 2(a). The radius of the outermost semi-ring nanoslit was set to 12.2 μm, and the radius of the innermost nanoslit was set to 8 μm. This structure was illuminated vertically by OAM beams with circular polarization from the bottom, and the power distribution of the OAM beams is uniform. Circularly polarized OAM beams are employed as incident light in this study, because they carry uniformly distributed electric fields along the azimuthal direction, and they are more stable compared with radially polarized OAM beams [46]. Figure 2(b) shows the electric field intensity ($|E|^2$) distribution of the BSW structure under an incident OAM beam with TC of one. A bright focal point appears around the center with a transverse shift. We focus on the central square region with an edge length of 3 μm [surrounded by a white dashed line in Fig. 2(b)]. Spatial phase patterns of OAM beams with TCs of two, four, six, eight, and ten (from top to bottom) are plotted in Fig. 2(c) (left), and the electric field intensity of the BSW structures under the corresponding incident OAM beams are shown in Fig. 2(c) (right). The white dashed
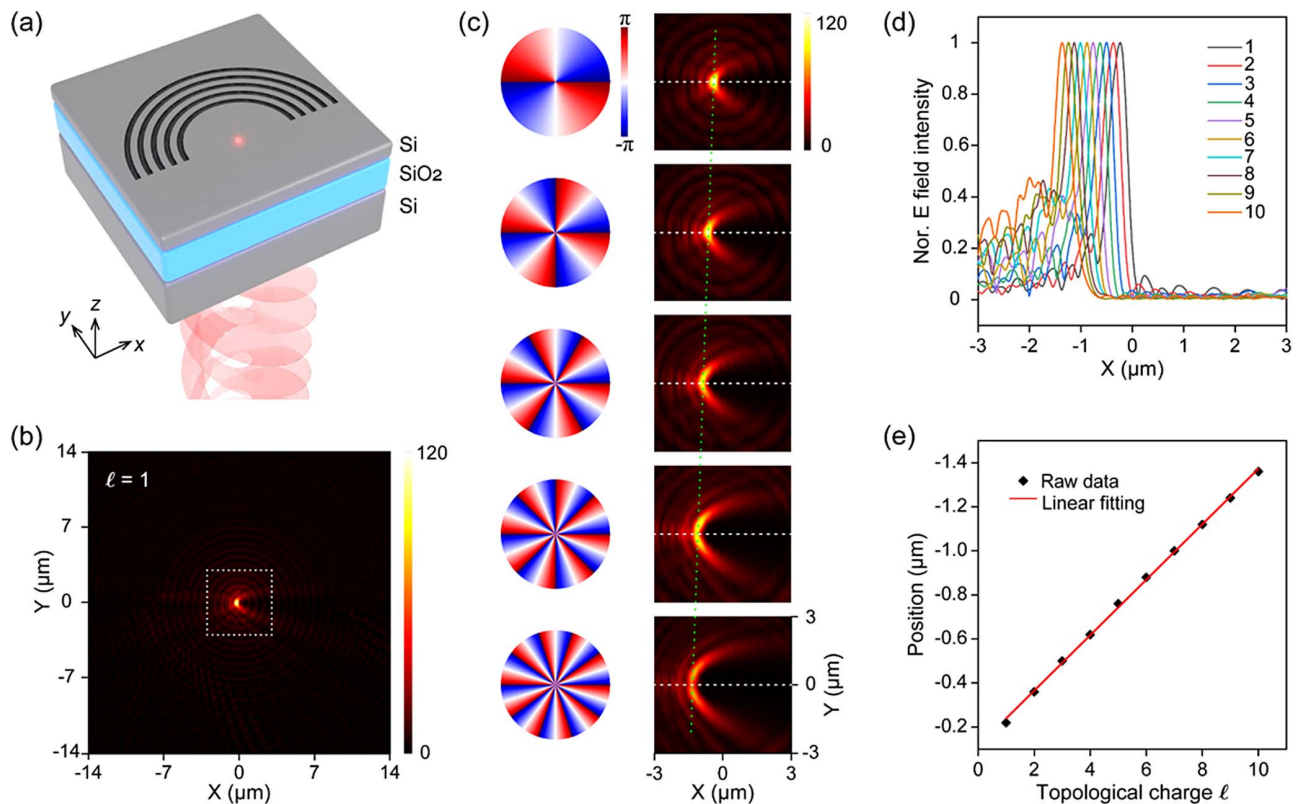
Fig. 2. On-chip sorting of OAM beams with different TCs using BSW structures. (a) Schematic of the designed BSW structure with five semiring shaped nanoslits. The structure was illuminated vertically by the OAM beam with circular polarization from the bottom. (b) Electric field intensity ($|E|^2$) of the BSW structure under incident OAM beam with TC of one. The edge length of the square region surrounded by the white dashed line is 3 μm. (c) Spatial phase patterns of OAM beams with TCs of two, four, six, eight, and ten (from top to bottom) (left) and the electric field intensity of the BSW structures under the corresponding incident OAM beams (right). All the subfigures share the same scale bar. The white dashed line indicates the position where $Y = 0$. The green dashed line indicates the peak position of the focal points. (d) Normalized electric field intensity along the white dashed lines in (c) under incident OAM beams with TCs of one to ten. (e) Linear fitting of the peak positions of the focal points as a function of the TCs of incident OAM beams. R^2 for this linear fitting is 0.999.

lines indicate the positions where $Y = 0$. Figure 2(d) shows the normalized electric field intensity along the white dashed lines under incident OAM beams with TCs of one to ten. It clearly shows that the incident OAM beams with larger TCs can lead to a larger transverse shift of the peak positions of the focal points, which is consistent with our former analysis. Figure 2(e) shows the peak positions of the focal points as a function of the TCs of incident OAM beams. A linear fitting is performed, and R^2 for this linear fitting is 0.999. The result reveals that a spatial interval of 135 nm on the chip between two neighboring OAM states can be obtained in this method.

As a comparison, on-chip sorting of OAM beams using a metallic structure is also investigated. The metallic structure for exciting SPPs is schematically sketched in Fig. 3(a). This structure consists of an Au film (top) and a SiO$_2$ substrate (bottom). The dielectric function of Au at 1.55 μm was set as $\varepsilon_{Au} = -116.62 + 11.46i$. The refractive index of SiO$_2$ at 1.55 μm was set as $1.47 + 0.005i$. The thickness of Au film was set as 0.2 μm. Similarly, five semi-ring shaped nanoslits were introduced on the top surface of this structure. The depth of the nanoslits was set as 0.2 μm, and the width of the nanoslits was set as 0.6 μm. The period of the nanoslits (the radial distance between two neighboring slits) was set to be

the effective wavelength of the SPPs. The effective wavelength of the SPPs can be calculated as [60]

$$\lambda_{SPP} = \mathrm{Re}\left[2\pi \middle/ \left(\frac{\omega}{c_0}\sqrt{\frac{\varepsilon_d \varepsilon_m}{\varepsilon_d + \varepsilon_m}}\right)\right], \quad (4)$$

where ω is the angular frequency of the incident light, c_0 is the speed of light in free space, and ε_d and ε_m are the dielectric function of air and the Au film, respectively. λ_{SPP} is calculated to be 1.543 μm. In this study, the period of the nanoslits on the metallic structure was set to 1.54 μm. The radius of the outermost semi-ring nanoslit on the metallic structure was set as 12.2 μm (the same as that on the BSW structure), and the radius of the innermost nanoslit was set as 6.04 μm. This structure was illuminated vertically by OAM beams with circular polarization from the bottom. Electric field intensity ($|E|^2$) of the metallic structure under an incident OAM beam with TC of one is plotted in Fig. 3(b). Similar to the case of the BSW structure, there is a focal point around the center with a transverse shift. The difference is that the electric field intensity at the focal point is relatively low. Spatial phase patterns of OAM beams with TCs of one, two, three, four, and five (from top to bottom) are plotted in Fig. 3(c) (left), and the electric
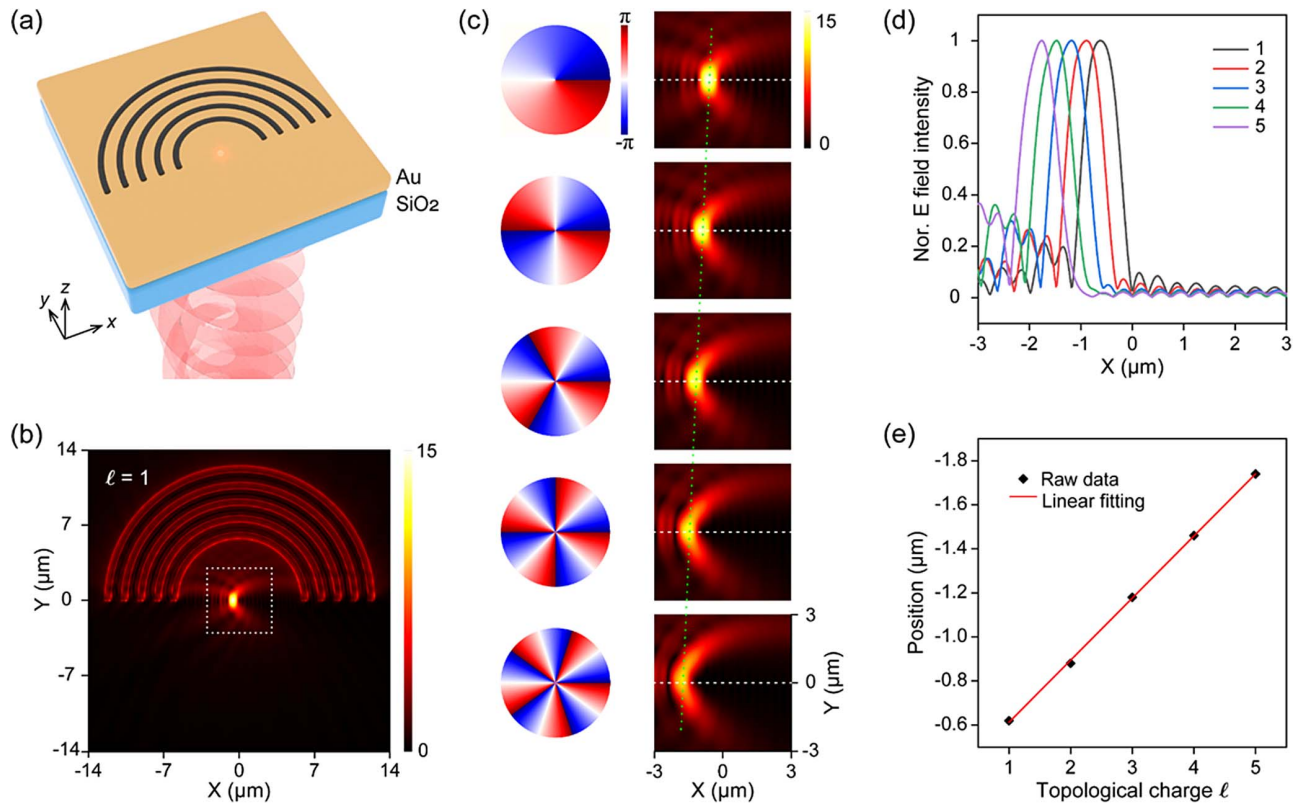
Fig. 3. On-chip sorting of OAM beams with different TCs using metallic structures. (a) Schematic of the metallic structure with five semi-ring nanoslits. This structure consists of an Au film (top) and a SiO_2 substrate (bottom). The structure was illuminated vertically by the OAM beam with circular polarization from the bottom. (b) Electric field intensity ($|E|^2$) of the metallic structure under incident OAM beam with TC of one. The edge length of the square region surrounded by the white dashed line is 3 μm. (c) Spatial phase patterns of OAM beams with TCs of one, two, three, four, and five (from top to bottom) (left) and electric field intensity of the metallic structure under the corresponding incident OAM beams (right). All the subfigures share the same scale bar. The white dashed line indicates the position where $Y = 0$. The green dashed line indicates the peak position of the focal points. (d) Normalized electric field intensity along the white dashed lines in (c) under incident OAM beams with TCs of one to five. (e) Linear fitting of the peak positions of the focal points as a function of the TCs of incident OAM beams. R^2 for this linear fitting is 0.997.

field intensity of the metallic structure under the corresponding incident OAM beams is shown in Fig. 3(c) (right). The white dashed lines indicate the positions where $Y = 0$. Figure 3(d) shows the normalized electric field intensity along the white dashed lines under incident OAM beams with TCs of one to five. It shows that as the TC of the incident OAM beams becomes larger, the peak position of the focal point shifts to the left gradually. The peak positions of the focal points as a function of the TCs of incident OAM beams are plotted in Fig. 3(e). A linear fitting is performed, and R^2 for this linear fitting is 0.997. A spatial interval of 270 nm on the chip between two neighboring OAM states can be obtained using this metallic structure.

The detection limits of OAM beams using metallic and BSW structures are carefully investigated. Figure 4(a) shows the electric field intensity of the metallic structure under an incident OAM beam with TCs of one, seven, and eight. We focus on the central line where $Y = 0$ since the peak position of focal points lies in this line (green dashed line). The electric field intensity of metallic structure under an incident OAM beam with other TCs (two to twelve) is shown in Appendix B. When the metallic structure is illuminated by an OAM beam

with TC not larger than seven, the electric field intensity at the focal point is the largest peak. When the TC of an incident OAM beam is greater than seven, however, the electric field intensity at the focal point is not the largest peak. In these cases, we cannot distinguish the peak positions of the focal points by simply examining the largest peaks of the electric field intensity along the central line. In this study, we set the detection criterion as follows: the electric field intensity at the focal point is the largest peak. Therefore, the detection limit of OAM beams using a metallic structure is seven. As a comparison, Fig. 4(b) shows the electric field intensity of the BSW structure under an incident OAM beam with TCs of 1, 35, and 36. The electric field intensity of the BSW structure under an incident OAM beam with other TCs (10–40) is also presented in Appendix B. When the BSW structure is illuminated by an OAM beam with TC not larger than 35, the electric field intensity at the focal point is the largest peak. When the TC of an incident OAM beam is greater than 35, however, the electric field intensity at the focal point is not the largest peak. Using the same detection criterion, we find the detection limit of OAM beams using the BSW structure is up to 35, which is much larger than that of the metallic structure (only seven).
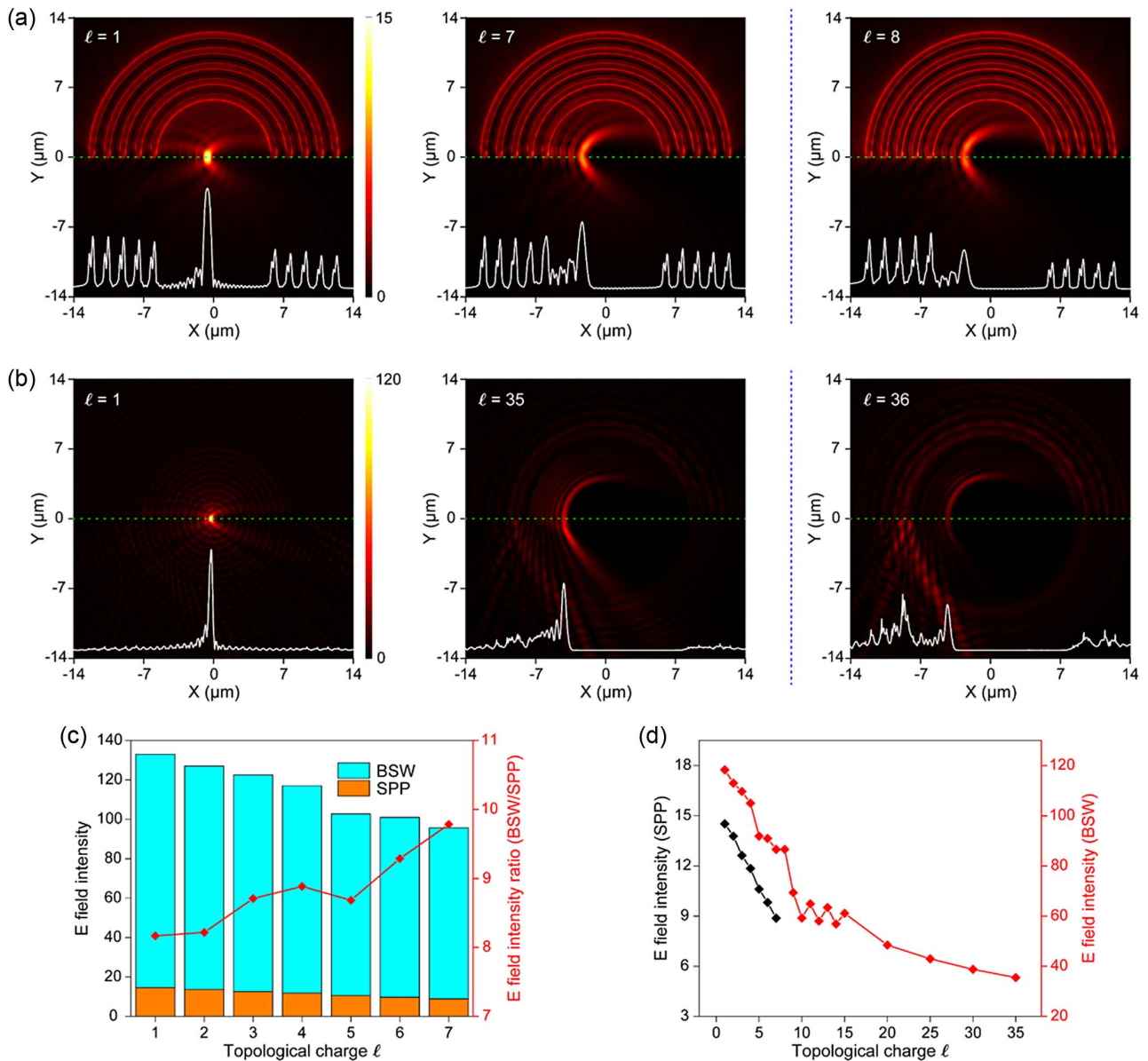
Fig. 4. Comparison of the electric field intensity ($|E|^2$) of the metallic structure and the BSW structure under incident OAM beams. (a) Electric field intensity of the metallic structure under incident OAM beams with TCs of one, seven, and eight. Subfigures in (a) share the same color scale bar. (b) Electric field intensity of the BSW structure under incident OAM beams with TCs of 1, 35, and 36. Subfigures in (b) share the same color scale bar. The green dashed lines in (a) and (b) indicate the position where $Y = 0$. The white curves in (a) and (b) refer to the electric field intensity along the green dashed line. (c) Electric field intensity of the focal points on metallic structure (SPP, orange) and BSW structure (cyan) under incident OAM beams with TCs of one to seven. Electric field intensity of the focal points on BSW structure over that on metallic structure is also plotted. (d) Electric field intensity of the focal points on metallic structure (SPP, black) under incident OAM beams with TCs of one to seven and electric field intensity of the focal points on BSW structure (red) under incident OAM beams with TCs of 1 to 35.

The reason for the large detection limit of OAM beams using the BSW structure is further explored. The electric field intensity of the metallic structure and the BSW structure is quantitatively calculated by averaging the intensity at a small region (0.1 μm × 0.1 μm) around the peak position of the focal point. As Fig. 4(c) shows, the electric field intensity of the focal points on the BSW structure is much higher than that on the metallic structure under an incident OAM beam with the same TC. For incident OAM beams with TCs of one to seven, the ratios of electric field intensity of the BSW structure to that of

the metallic structure are 8.17, 8.22, 8.71, 8.88, 8.68, 9.29, and 9.78, respectively. The electric field intensity of metallic and BSW structures along the central line where $Y = 0$ under an incident OAM beam with different TCs is presented in detail in Appendix B. The electric field intensity of the focal points of metallic and BSW structures is summarized in Fig. 4(d). We can see that the electric field intensity of the focal points decreases with the increase of the TC of the incident OAM beam. For the BSW structure, the electric field intensity of the focal points decreases rapidly when the TC of the

incident OAM beam is small (<10), while it decreases slowly when the TC of the incident OAM beam gets large (>20).

The electric field intensity of focal points on the BSW structure is much higher than that of the metallic structure (over eight times). The reason for this is explained below. Since the BSW structures consist of several dielectric layers, absorption loss of BSWs is much lower in comparison with that of SPPs [50–52]. To examine the contribution of the absorption loss, a low-loss artificial "ideal" material is modeled. The dielectric function of this artificial material is set as $\varepsilon_a = -116.62 + 0.01i$. As a comparison, the dielectric function of Au at 1.55 μm is $\varepsilon_{Au} = -116.62 + 11.46i$. The effective wavelength of this artificial material is 1.54 μm. The electric field intensity of the artificial structure with five nanoslits under different incident OAM beams is presented in Appendix C. The radius of the outermost nanoslit is 12.2 μm. Using the same detection criterion, the detection limit of OAM beams using this artificial structure is 13. When the focal point approaches the innermost nanoslit, the energy transfers to the nanoslit and the detection limit is severely restricted. It appears that the nanoslit with a relatively small radius limits the number of TCs that can be detected, but it is appropriate to increase the radius of the nanoslits since the attenuation of the "ideal" material is so low. The size of this structure is further increased, and its electric field intensity under different incident OAM beams is also shown in Appendix C. The radius of the outermost nanoslit is 18.36 μm, and the detection limit of OAM beams increases dramatically to 26. Since the real part of the dielectric function of this artificial material is the same as that of the Au, this result demonstrates that the low-absorption-loss property of the material is the major contribution to the larger detection limit. The reason for the difference between the "ideal" material and the BSW lies in the difference in the effective wavelengths of the different wavemodes. The effective wavelength of BSWs (1.05 μm) is smaller than that of SPPs (1.54 μm). The smaller effective wavelength results in a stronger focusing ability (the ability to focus energy to a small spot), which causes a smaller spot size and higher energy density at the spot size [61,62]. Taken together, the low absorption loss and smaller effective wavelength are the reasons for the larger detection limit of OAM beams using the BSW structure (35) than that using the metallic structure (7).

In addition, the full width at half-maximum (FWHM) of electric field intensity of the metallic structure and BSW structure under incident OAM beams with different TCs is summarized in Table 1. FWHM of electric field intensity of the BSW structure is much smaller (approximately one half) than that of the metallic structure. The reason can be ascribed to the smaller effective wavelength of BSWs (1.05 μm) than that of SPPs (1.54 μm). The smaller effective wavelength results in a stronger focusing ability, which causes a smaller spot size and

smaller FWHM of electric field intensity [61,62]. FWHM of electric field intensity of the BSW structure does not get broadened with the increase of the TC of the OAM beam. Although the FWHM of electric field intensity does not affect the detection limit directly, it can provide higher resolution for the detection. The improvement of detection resolution is essential for optical multiplexing systems that exploit the orthogonality of the OAM modes, especially for sorting multiple OAM beams simultaneously [43]. Taken together, BSW structures exhibit better OAM sorting performances than SPPs in terms of higher electric field intensity and smaller FWHM, which is beneficial for OAM sorting with large TCs. BSW structures are therefore a suitable and promising alternative for OAM sorting with large TCs.

The above discussion is based on the condition that only one OAM beam is illuminated on the BSW structure. On the other hand, sorting of two or several OAM beams simultaneously is of vital importance to OAM demultiplexing and optical communication. To our knowledge, however, the demonstration of on-chip sorting of two OAM beams simultaneously has never been reported. Electric field intensity of the BSW structure under an incident OAM beam with TC of –3 is presented in Fig. 5(a) for comparison. Figure 5(b) shows the electric field intensity of the BSW structure under the incidence of two OAM beams with TCs of 1 and –3. Two focal points can be barely observed in this case. The positions of the focal points are quantitatively analyzed in Figs. 5(c)–5(e). For incident OAM beams with TCs of 1 and –3, the positions of these two focal points are $X = -0.24$ μm and 0.3 μm [Fig. 5(c)], respectively. There is a dip between these two points. Since the position of the first focal point is beyond the first-order dark ring of the second focal point, these two focal points can be barely separated according to the Rayleigh criterion. Therefore, to separate two OAM beams, a difference of at least four for TCs is required. For incident OAM beams with TCs of 3 and –3, the intensity of the dip between the two focal points approaches zero [Fig. 5(d)], so these two focal points can be completely separated. For incident OAM beams with TCs of 5 and –3, the dip between the intensity of these two focal points is rather broad. Both the positions and intensities of these two focal points are approximately the same as the positions and intensities of the focal points generated by a single OAM beam [Fig. 5(e)]. In all these cases, the positions of these two focal points coincide with that of the focal point generated by a single OAM beam. Taken together, on-chip sorting of two OAM beams simultaneously using BSW structures can be achieved as long as the difference between these two TCs is no less than four, and the positions of these two focal points are the same as that of the focal points generated by a single OAM beam. By examining the positions of the two focal points, the information of the two incident OAM beams can be easily

Table 1. Full Width at Half-Maximum of Electric Field Intensity Distribution of the Metallic Structure and BSW Structure under Incident OAM Beams with Different TCs

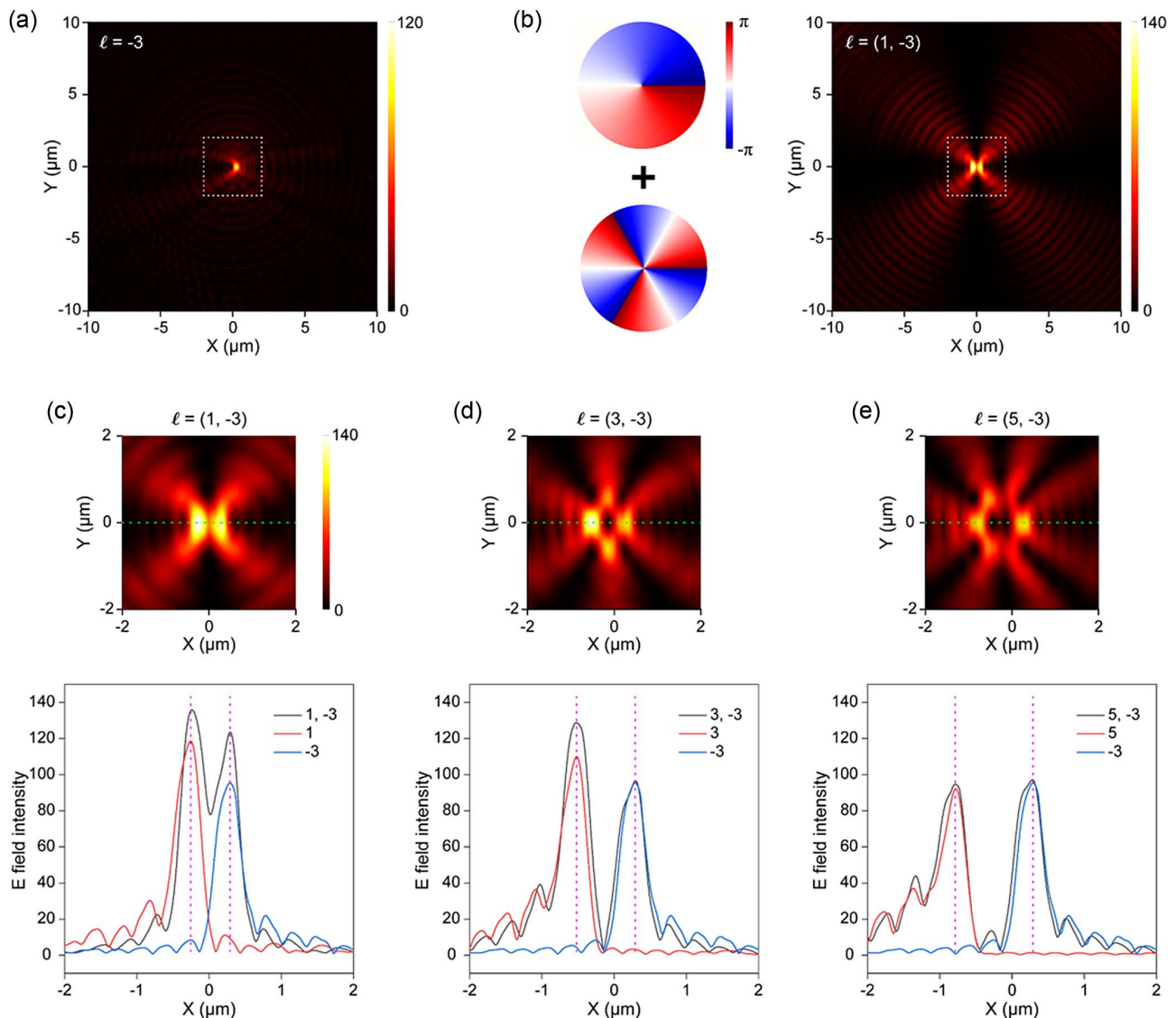| TC	1	2	3	4	5	6	7	8	9	10
FWHM (SPP) (μm)	0.78	0.78	0.78	0.80	0.80	0.82	0.82			
FWHM (BSW) (μm)	0.42	0.42	0.42	0.42	0.42	0.42	0.40	0.40	0.40	0.40

Fig. 5. On-chip sorting of two OAM beams simultaneously. (a) Electric field intensity of the BSW structure under the incident OAM beam with TC of –3. The edge length of the square region surrounded by the white dashed line is 2 μm. (b) Spatial phase patterns of OAM beams with TCs of 1 and –3 (from top to bottom) (left) and electric field intensity of the BSW structure under the incidence of two OAM beams with TCs of 1 and –3 (right). The edge length of the square region surrounded by the white dashed line is 2 μm. (c) Electric field intensity of the BSW structure under the incidence of two OAM beams with TCs of 1 and –3 (top), and the electric field intensity along the green dashed line (bottom). (d) Electric field intensity of the BSW structure under the incidence of two OAM beams with TCs of 3 and –3 (top), and the electric field intensity along the green dashed line (bottom). (e) Electric field intensity of the BSW structure under the incidence of two OAM beams with TCs of 5 and –3 (top), and the electric field intensity along the green dashed line (bottom); (c)–(e) share the same color scale bar. The green dashed line indicates the position where $Y = 0$. The purple dashed lines indicate the peak positions of the two focal points.

recovered. The above discussion is based on two incident beams with the same polarization state (circular polarization). However, if the polarization states of the two incident beams are different from each other (linear polarization and circular polarization), the sorting of the two OAM beams would still work, but the sorting performance is worse than sorting two OAM beams with the same polarization state (circular polarization).

The reason for choosing five semi-ring shaped nanoslits is explained below. As we mentioned before, the period of the nanoslits was fixed at 1.05 μm to enhance the energy at the

focal point. Figure 6(a) shows the electric field intensity of the BSW structure with five semi-ring nanoslits. This structure was illuminated by a circularly polarized OAM beam with TC of one from the bottom. A bright focal point can be clearly observed around the center with a transverse shift. We focus on the central square region with edge lengths of 2 μm (surrounded by the white dashed line). The BSW structures with one to six semi-ring shaped nanoslits are schematically plotted in Fig. 6(b) (top), and the electric field intensities of the corresponding structures under incident OAM beams is shown in Fig. 6(b) (bottom). It shows that the peak positions of the focal
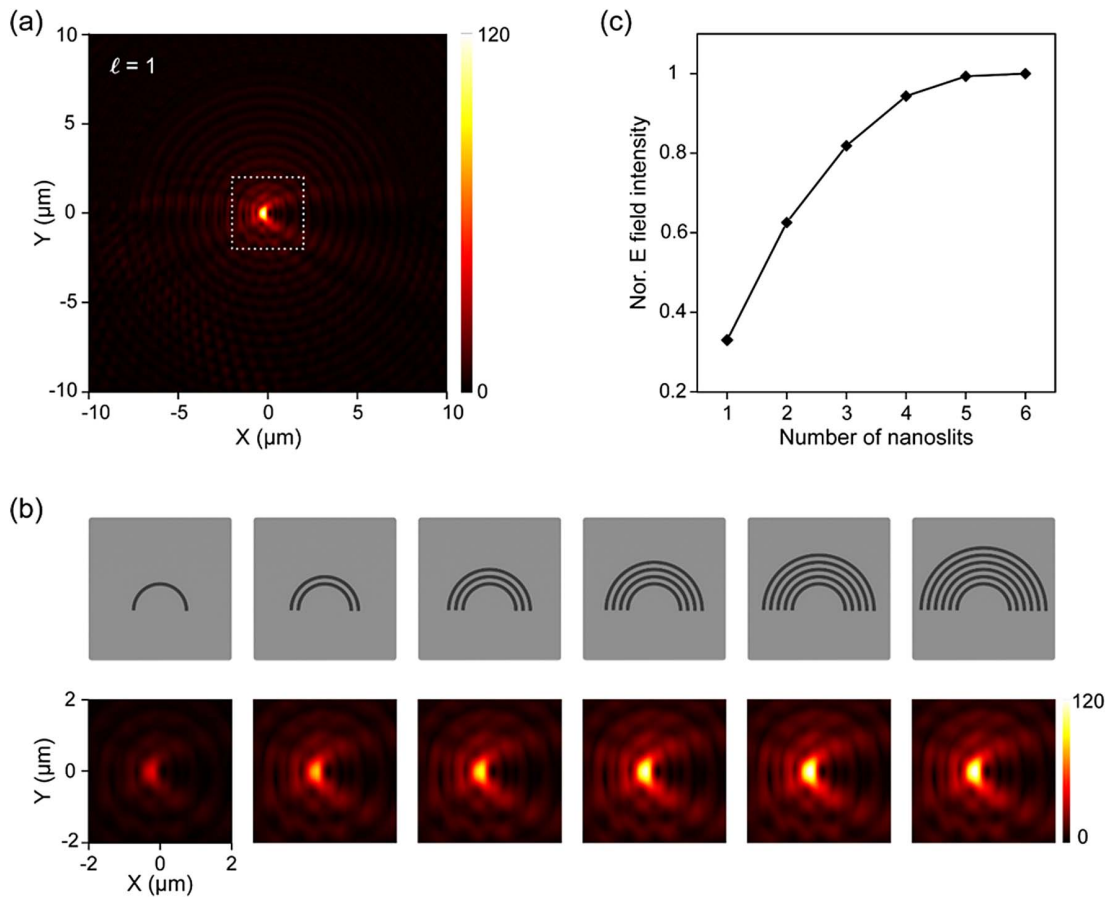
Fig. 6. Comparison of BSW structures with different semi-ring shaped nanoslits. (a) Electric field intensity of the BSW structure with five semi-ring nanoslits. The structure was illuminated by a circularly polarized OAM beam with TC of one from the bottom. The edge length of the square region surrounded by the white dashed line is 2 μm. (b) Schematic of the BSW structures with one to six semi-ring shaped nanoslits (top) and the electric field intensity of the corresponding structures (bottom) under incidence of an OAM beam with TC of one. All the subfigures share the same scale bar. (c) Normalized electric field intensity of the region around the peak positions of focal points as a function of nanoslit numbers.

points of the BSW structures with different nanoslits remain the same, while the electric field intensity of the focal points increases gradually. The electric field intensity is quantitatively calculated by averaging the intensity at a small region around the focal point (0.1 μm × 0.1 μm), as plotted in Fig. 6(c). It clearly shows that the electric field intensity of the BSW structures becomes larger when the nanoslit number increases, but it gets saturated gradually. The electric field intensity of the BSW structure with five nanoslits is 99.3% that of the structure with six nanoslits. The scattering loss caused by the inner nanoslits is the main reason. The transmission coefficient t is defined as the percentage of the energy that can reach the focal point after scattering by the inner nanoslit. The transmission coefficient t of each nanoslit is calculated to be 0.383. Therefore, the ratio of the electric field intensity of the five-nanoslit structure to that of the six-nanoslit structure can be thought of as the ratio between two geometric series with five and six terms, respectively. The ratio is $(1 - t^5)/(1 - t^6) = 0.995$, which is consistent with the result in Fig. 6(c). To make a balance between high electric field intensity and a small footprint, the BSW structures with five semi-ring shaped nanoslits were employed throughout this study.

The contributions from different electric field components ($|E_x|$, $|E_y|$, and $|E_z|$) are further analyzed. Electric field components of BSW and metallic structures under incident OAM beams with TC of five are presented in Appendix D. For the BSW structure, it can be clearly observed that the magnitudes of in-plane electric field components ($|E_x|$ and $|E_y|$) are much larger than that of the out-of-plane electric field component ($|E_z|$). It proves that the BSW is excited by the TE polarization. On the contrary, for the metallic structure, the magnitudes of $|E_x|$ and $|E_y|$ are much smaller than that of $|E_z|$, which proves that the SPP is excited by the TM polarization. Although we only perform numerical simulations in this study, we propose the possible methods to measure the positions of the focal points in experiments. Near-field scanning optical microscopy (NSOM) with spatial resolution below the diffraction limit is a powerful technique, which has been used to characterize nano-structures with complex morphologies. The typical spatial resolution of an NSOM system is around 10–20 nm [63,64], which is capable of measuring the positions of the focal points in this study. Depending on the characteristics of the probes, NSOM can be generally divided into two approaches. Aperture-type NSOM employs optical fibers as probes, and it is

sensitive to the in-plane electric field component [65–67]. An aperture-type NSOM system can therefore be used to measure the focal points on the BSW structures. In contrast, apertureless NSOM employs machined tips (such as metallic nanoparticles) as probes, which is more sensitive to the out-of-plane electric field component [65–67]. An apertureless NSOM system can be used to measure the focal points on the metallic structures.

4. CONCLUSION

In summary, on-chip sorting of OAM beams using BSW structures is numerically investigated in this study. The designed BSW structures consist of three dielectric layers, which are Si (top), SiO_2 (middle), and Si substrate (bottom). Several semi-ring shaped nanoslits were introduced on the top surface of the BSW structures, and the number of nanoslits was optimized to be five. BSWs can be excited and modulated by the helical phase wavefront of the incident OAM beams. There is a transverse shift for the focal point owing to the constructive interference of the BSWs. An on-chip spatial interval of 135 nm between two neighboring OAM states can be obtained by using BSW structures. Furthermore, OAM sorting behaviors of metallic structures with the same morphology are also analyzed. OAM beams with TCs up to 35 can be successfully sorted by the BSW structures. As a comparison, it is difficult to detect OAM beams with TCs larger than seven by using metallic structures. BSW structures exhibit better OAM sorting performances than SPPs in terms of higher electric field intensity and smaller FWHM, which is beneficial for OAM sorting with large TCs. In addition, sorting of two OAM beams simultaneously can be achieved in this way as long as the difference between these two TCs is no less than four. By employing an ideal lossless material, we demonstrate that the greatly reduced loss of the BSW structure accounts for a big improvement of the detection limit from TC of 7 to TC of 26; the remaining improvement accounts for the smaller effective wavelength of the BSWs, which results in a tighter and more intense focus. To our knowledge, this is the first demonstration of on-chip sorting of OAM beams with TCs up to 35 as well as the first report of on-chip sorting of two OAM beams simultaneously. Our results reveal that BSW structures can be a remarkable solution for OAM sorting with large TCs. The investigation of BSWs will undoubtably broaden the OAM sorting strategies, and will be potentially applied in optical field manipulation, integrated photonic circuits, optical communications, and on-chip device design.

APPENDIX A: MECHANISM OF OAM SORTING

The mechanism of the orbital angular momentum (OAM) sorting methods is schematically illustrated in Fig. 1(d). We first consider the case of only one nanoslit. Assuming the incident light possesses a phase profile of $\exp(il\varphi)$ with radial polarization, the electric field at the surface can be expressed as [46]

$$E(r,\varphi) = \int_0^\pi |\vec{r}_0 - \vec{r}|^{-\frac{1}{2}} \exp(il\varphi) \exp(ik_{BSW}|\vec{r}_0 - \vec{r}|) d\varphi,$$

(A1)

where $\vec{r}$ is the position vector of the observing point P. $\vec{r}_0$ is the position vector of an arbitrary point on the semi-ring nanoslit. l denotes the topological charge (TC) of the incident OAM beams. φ is the azimuthal angle. k_{BSW} refers to the wavevector of the Bloch surface wave (BSW). Due to the helical phase of the OAM beams, the phase along the semi-ring nanoslit has a linear dependence on the azimuthal angle φ. In this case, the excited BSWs do not focus at the original point O, and there is a transverse shift for the focal region. Since the size of the focal region is much smaller than the diameter of the semi-ring nanoslit, the focal region can be treated as a single point. The above equation can be further expressed as [68,69]

$$E(x) \propto J_l(k_{BSW}x),$$

(A2)

where J_l is the lth-order Bessel function. The transverse peak position of the focal point can therefore be derived to

$$x_l = \mathrm{sgn}(l)\frac{\mu_l}{k_{BSW}}.$$

(A3)

The above equation can be further simplified to

$$x_l = \mathrm{sgn}(l)\frac{\mu_l}{2\pi}\lambda_{BSW},$$

(A4)

where μ_l is the first non-zero coefficient of $J_l'(x)$ [the derivative of $J_l(x)$] and $\mu_{l=0} = 0$; λ_{BSW} is the effective wavelength of BSW. According to Eq. (A4), the transverse peak position of the focal point is only determined by l and λ_{BSW}, since μ_l is fixed for a specific material.

When the incident light is a plane wave ($l = 0$), the excited BSW focuses at the original position O. For incident OAM beams with positive TC ($l > 0$), the excited BSWs focus at the left side of O. Correspondingly, for incident OAM beams with negative TC ($l < 0$), the excited BSWs focus at the right side of O due to symmetry. In addition, incident OAM beams with a larger absolute value of TC $|l|$ result in a larger transverse shift of peak position $|x|$.

For multiple semi-ring nanoslits with different radii, the transverse position of the focal point remains the same since Eq. (A4) is independent of the radius of the nanoslit. The electric field intensity at the focal point can be enhanced or weakened depending on the phase differences of the BSWs excited by different nanoslits. Therefore, the period of the nanoslits (the radial distance between two neighboring slits) was set to be λ_{BSW} to enhance the electric field intensity at the focal point.

In addition, the above analysis of the OAM sorting mechanism can be further extended to linearly polarized and circularly polarized incident light. For linearly polarized light with fixed polarization angle ζ, the electric field vector can be decomposed into two components. One component is along the radial direction, and the other component is perpendicular to the radial direction. Since only the component along the radial direction can excite BSWs, only this component will be considered. The electric field at the surface can be expressed as

$$E(r,\varphi)$$
$$= \int_0^\pi |\vec{r}_0 - \vec{r}|^{-\frac{1}{2}} \cos(\zeta - \varphi) \exp(il\varphi) \exp(ik_{BSW}|\vec{r}_0 - \vec{r}|) d\varphi. \quad \textbf{(A5)}$$

In the direction where $\varphi = \zeta$ or $\varphi = \zeta \pm \pi$, the electric field reaches the maximum value. In the direction where

$\varphi = \zeta \pm 2/\pi$, the electric field becomes zero. The overall integral of the electric field under linear polarization is obviously smaller than that under radial polarization.

For circularly polarized light, the phase item can be expressed as $\exp[i(l + s)\varphi]$, where s denotes the spin angular momentum (SAM). Both OAM and SAM can contribute to a transverse shift of the position of the focal point. In this case, the electric field at the surface can be expressed as

$$E(r,\varphi) = \int_0^{\pi} |\vec{r}_0 - \vec{r}|^{-\frac{1}{2}} \exp[i(l + s)\varphi] \exp(ik_{\mathrm{BSW}}|\vec{r}_0 - \vec{r}|)\mathrm{d}\varphi.$$

$$\textbf{(A6)}$$

Similarly, the transverse peak position of the focal point can be expressed as

$$x_j = \mathrm{sgn}(j)\frac{\mu_j}{2\pi}\lambda_{\mathrm{BSW}}, \qquad \textbf{(A7)}$$

where $j = l + s$, and j is the total angular momentum. s equals one for right-handed circular polarization (RCP), while s equals –1 for left-handed circular polarization (LCP). Since the circular polarization state of incident light can be fixed ($s = \pm 1$), the OAM can be derived from the total angular momentum ($l = j - s = j \pm 1$). Taken together, the mechanism of OAM sorting methods is valid for radially polarized, linearly polarized, and circularly polarized incident light.

APPENDIX B: OAM SORTING PERFORMANCE COMPARISON

OAM sorting performances of metallic structure and BSW structure are compared in Figs. 7–9. The electric field intensity of metallic structure under an incident OAM beam with TCs of 2, 4, 6, 9, 10, and 12 is shown in Fig. 7. The detection limit of OAM beams using this metallic structure is 7. As a comparison, the electric field intensity of BSW structure under an incident OAM beam with TCs of 10, 20, 30, 37, 38, and 40 is shown in Fig. 8. The detection limit of OAM beams using this BSW structure is 35. The electric field intensity of metallic structure and BSW structure along the central line under incident OAM beams with different TCs is further presented in Fig. 9. The electric field intensity of focal points on BSW structure is much higher than that of metallic structure (over eight times).

APPENDIX C: OAM SORTING PERFORMANCE OF THE ARTIFICIAL MATERIAL

The dielectric function of the artificial material is set as $\varepsilon_a = -116.62 + 0.01i$. The effective wavelength of this artificial material is 1.54 μm, and its electric field intensity under incident OAM beams with TCs of 5, 10, 12, 13, 14, and 15 is shown in Fig. 10. The radius of the outermost semi-ring nanoslit was 12.2 μm. The detection limit of OAM beams using this artificial material is 13. As a comparison, the electric
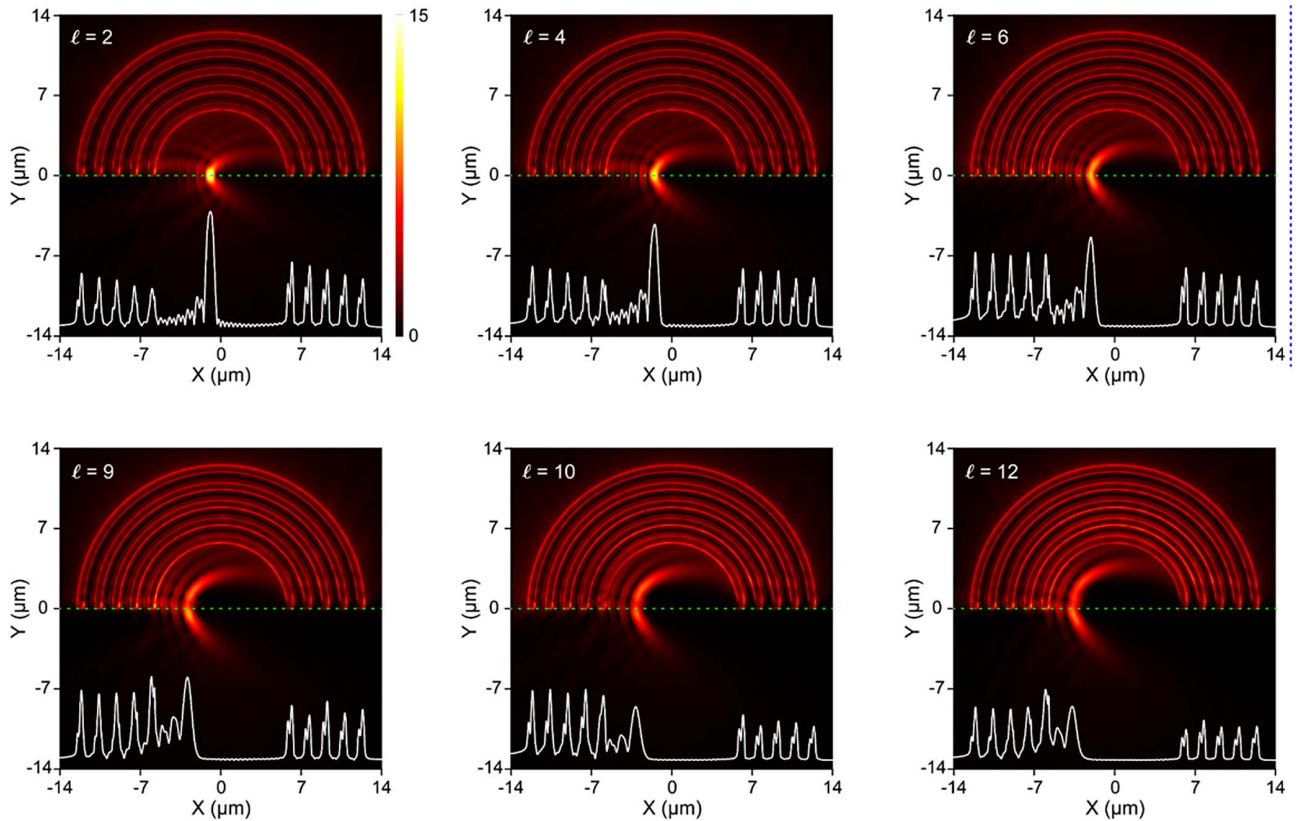

Fig. 7. Electric field intensity of the metallic structure under incident OAM beams with TCs of 2, 4, 6, 9, 10 and 12. The green dashed line indicates the position where $Y = 0$. The white curve refers to the electric field intensity along the green dashed line. All figures share the same color scale bar.
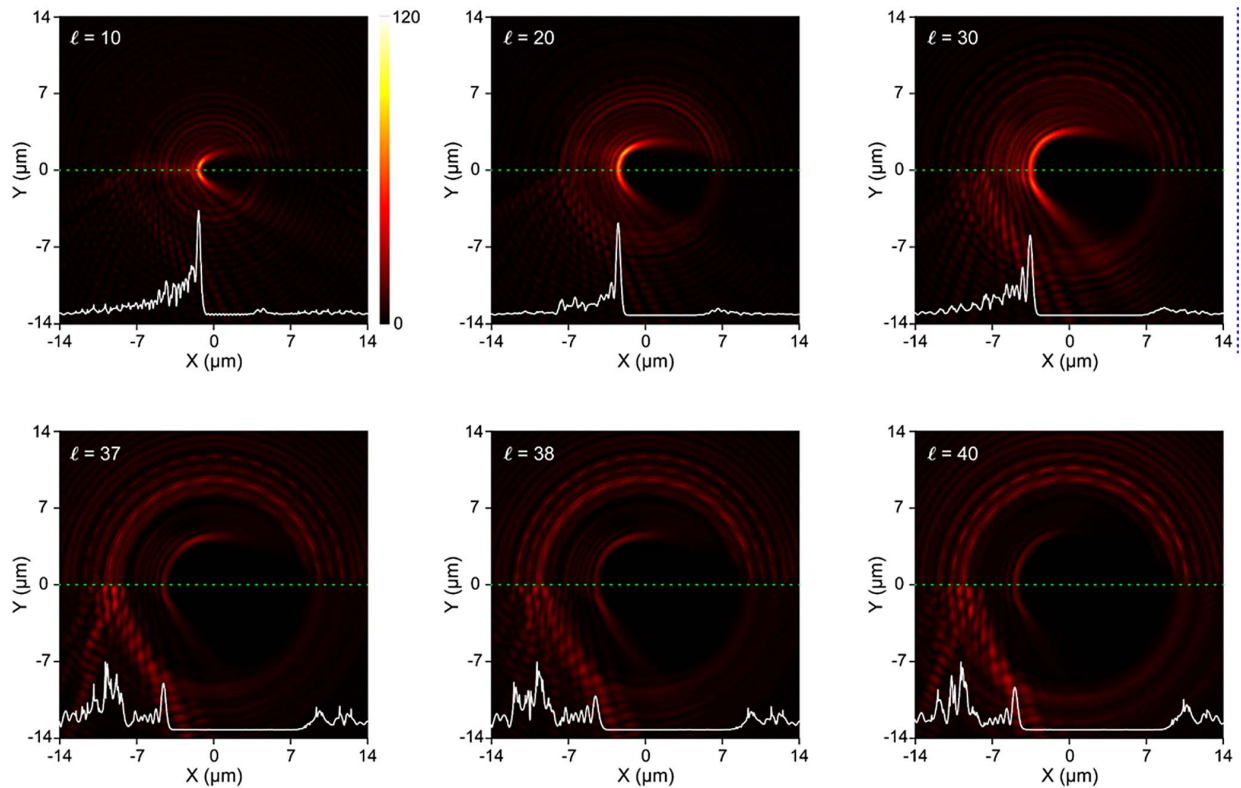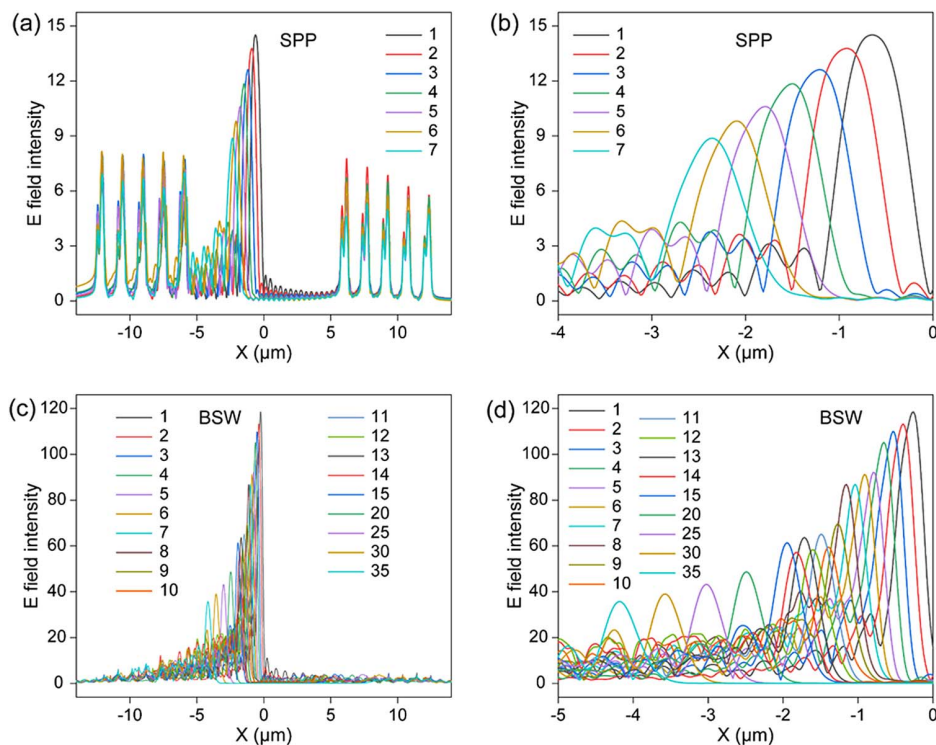
Fig. 8. Electric field intensity of the BSW structure under incident OAM beams with TCs of 10, 20, 30, 37, 38, and 40. The green dashed line indicates the position where $Y = 0$. The white curve refers to the electric field intensity along the green dashed line. All figures share the same color scale bar.

Fig. 9. (a), (b) Electric field intensity of the metallic structure along the $Y = 0$ line under incidence of OAM beams with TCs of 1 to 7 with a broader X-axis scale (a) and a narrower X-axis scale (b). (c), (d) Electric field intensity of the BSW structure along the $Y = 0$ line under incidence of OAM beams with TCs of 1 to 35 with a broader X-axis scale (c) and a narrower X-axis scale (d).
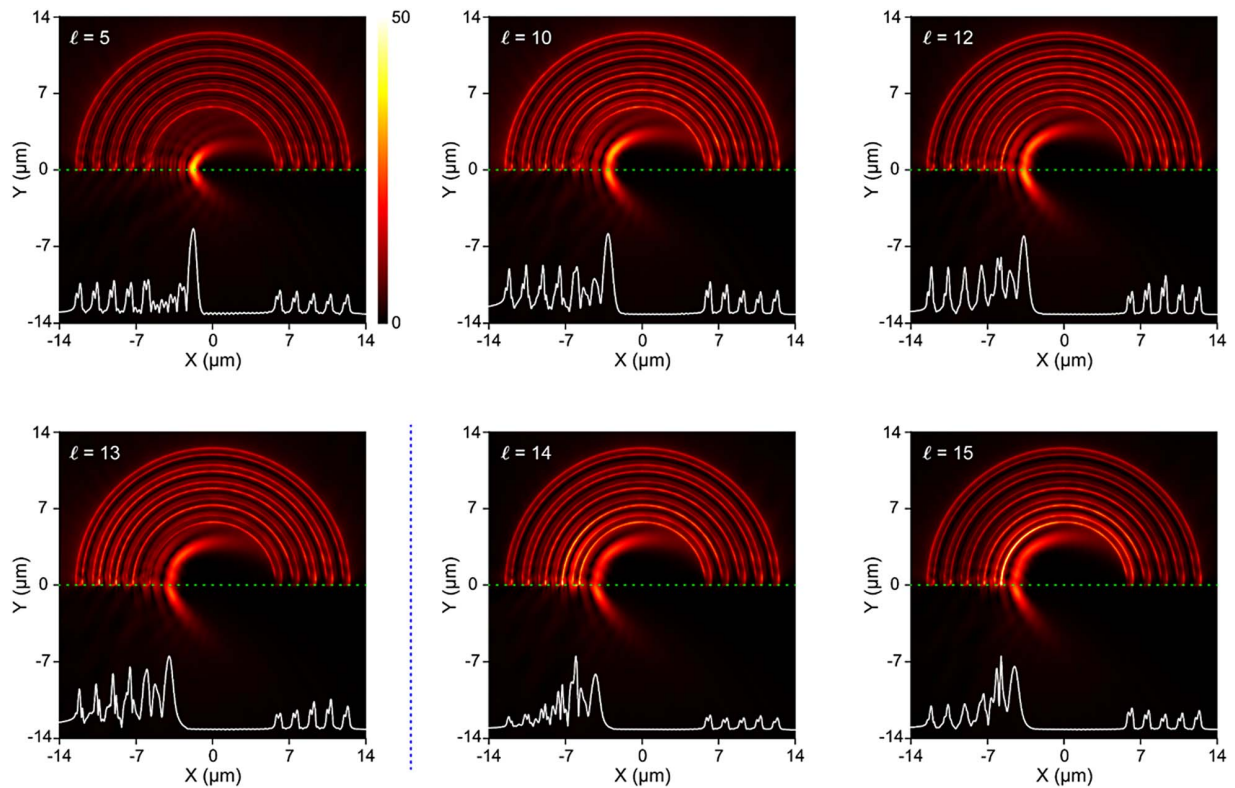
Fig. 10. Electric field intensity of the artificial structure under incident OAM beams with TCs of 5, 10, 12, 13, 14, and 15. The green dashed line indicates the position where $Y = 0$. The white curve refers to the electric field intensity along the green dashed line. All figures share the same color scale bar. The radius of the outermost semi-ring nanoslit is 12.2 μm.
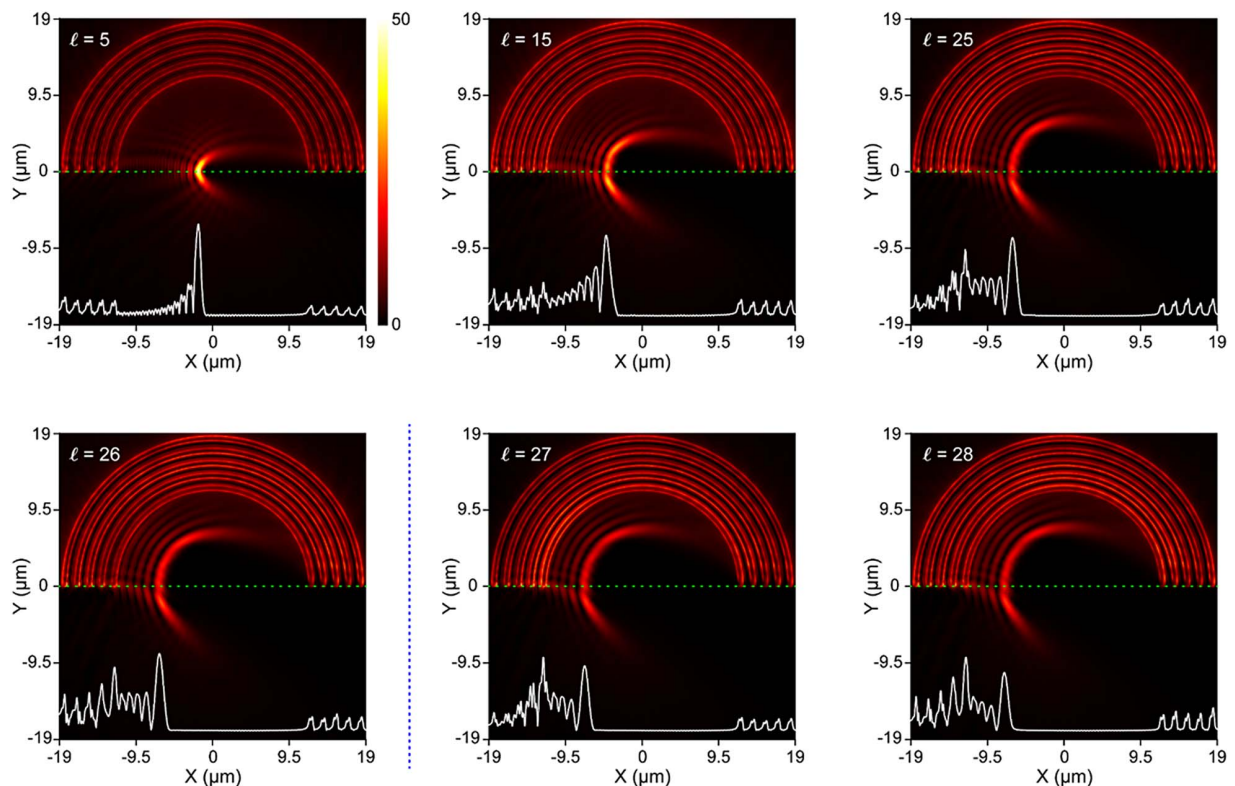

Fig. 11. Electric field intensity of the artificial structure with larger radius under incident OAM beams with TCs of 5, 15, 25, 26, 27, and 28. The green dashed line indicates the position where $Y = 0$. The white curve refers to the electric field intensity along the green dashed line. All figures share the same color scale bar. The radius of the outermost semi-ring nanoslit is 18.36 μm.
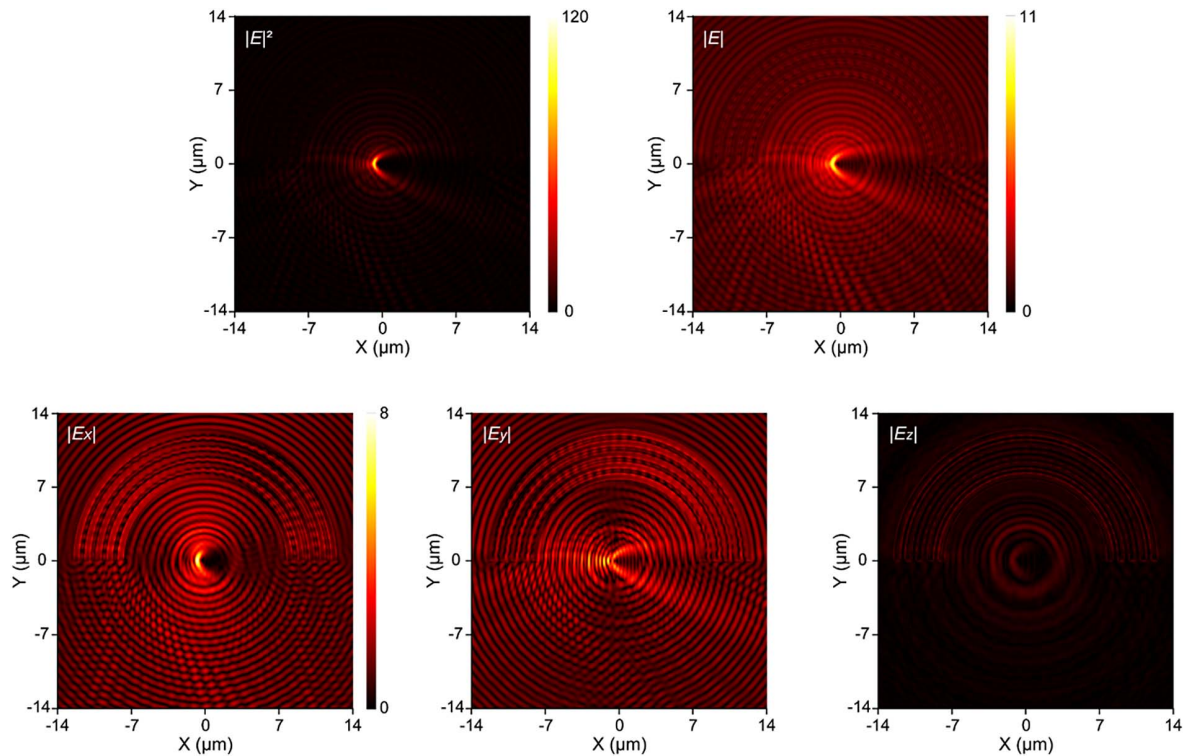
Fig. 12. Electric field intensity ($|E|^2$) and electric field components ($|E|$, $|E_x|$, $|E_y|$, and $|E_z|$) of the BSW structure under incident OAM beams with TC of five. The bottom three figures share the same color scale bar.
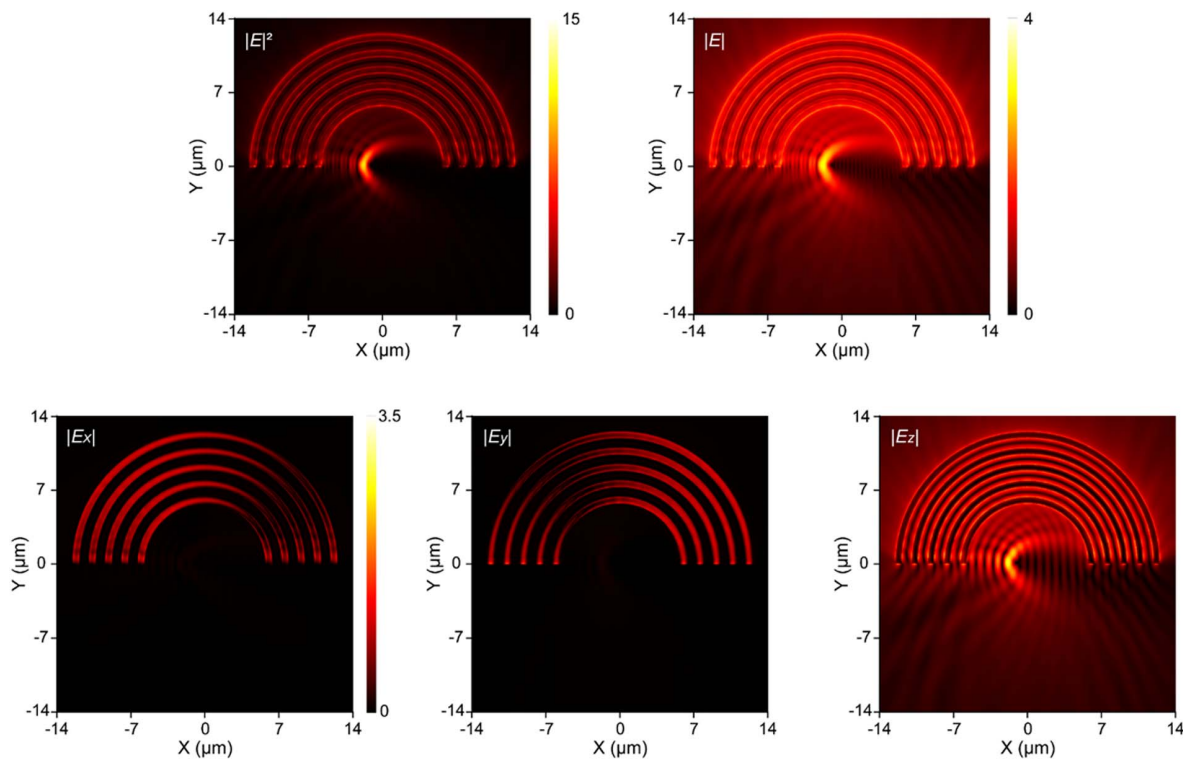

Fig. 13. Electric field intensity ($|E|^2$) and electric field components ($|E|$, $|E_x|$, $|E_y|$, and $|E_z|$) of the metallic structure under incident OAM beams with TC of five. The bottom three figures share the same color scale bar.

field intensity of this artificial material with larger radii under incident OAM beams with TCs of 5, 15, 25, 26, 27, and 28 is shown in Fig. 11. The radius of the outermost semi-ring nano-slit was 18.36 μm. The detection limit of OAM beams using this artificial material with larger radii is 26.

APPENDIX D: ELECTRIC FIELD COMPONENT ANALYSIS

Electric field components of BSW structure under incident OAM beams with a TC of 5 are shown in Fig. 12. For BSW structure, the magnitudes of $|E_x|$ and $|E_y|$ are much larger than that of $|E_z|$. It proves that the BSW is excited by the TE polarization. Electric field components of metallic structure under incident OAM beams with a TC of 5 are shown in Fig. 13. For metallic structure, the magnitudes of $|E_x|$ and $|E_y|$ are much smaller than that of $|E_z|$, which proves that the SPP is excited by the TM polarization.

Disclosures. The authors declare no conflicts of interest.

Data Availability. Data underlying the results presented in this paper are not publicly available at this time but may be obtained from the authors upon reasonable request.

REFERENCES

1. X. L. Cai, J. W. Wang, M. J. Strain, B. Johnson-Morris, J. B. Zhu, M. Sorel, J. L. O'Brien, M. G. Thompson, and S. Y. Yu, "Integrated compact optical vortex beam emitters," Science **338**, 363–366 (2012).
2. N. Bozinovic, Y. Yue, Y. X. Ren, M. Tur, P. Kristensen, H. Huang, A. E. Willner, and S. Ramachandran, "Terabit-scale orbital angular momentum mode division multiplexing in fibers," Science **340**, 1545–1548 (2013).
3. P. Miao, Z. F. Zhang, J. B. Sun, W. Walasik, S. Longhi, N. M. Litchinitser, and L. Feng, "Orbital angular momentum microlaser," Science **353**, 464–467 (2016).
4. Y. J. Shen, X. J. Wang, Z. W. Xie, C. J. Min, X. Fu, Q. Liu, M. L. Gong, and X. C. Yuan, "Optical vortices 30 years on: OAM manipulation from topological charge to multiple singularities," Light Sci. Appl. **8**, 90 (2019).
5. T. Lei, M. Zhang, Y. R. Li, P. Jia, G. N. Liu, X. G. Xu, Z. H. Li, C. J. Min, J. Lin, C. Y. Yu, H. B. Niu, and X. C. Yuan, "Massive individual orbital angular momentum channels for multiplexing enabled by Dammann gratings," Light Sci. Appl. **4**, e257 (2015).
6. J. Wang, "Advances in communications using optical vortices," Photonics Res. **4**, B14–B28 (2016).
7. J. Wang, J.-Y. Yang, I. M. Fazal, N. Ahmed, Y. Yan, H. Huang, Y. X. Ren, Y. Yue, S. Dolinar, M. Tur, and A. E. Willner, "Terabit free-space data transmission employing orbital angular momentum multiplexing," Nat. Photonics **6**, 488–496 (2012).
8. J. P. Cheng, X. B. Sha, H. Zhang, Q. M. Chen, G. Y. Qu, Q. H. Song, S. H. Yu, and S. M. Xiao, "Ultracompact orbital angular momentum sorter on a CMOS chip," Nano Lett. **22**, 3993–3999 (2022).
9. S. N. Khonina, N. L. Kazanskiy, M. A. Butt, and S. V. Karpeev, "Optical multiplexing techniques and their marriage for on-chip and optical fiber communication: a review," Opto-Electron. Adv. **5**, 210127 (2022).
10. J. X. Zhang, P. X. Li, R. C. C. Cheung, A. M. H. Wong, and J. Li, "Generation of time-varying orbital angular momentum beams with space-time-coding digital metasurface," Adv. Photonics **5**, 036001 (2023).
11. J. Chen, C. H. Wan, and Q. W. Zhan, "Engineering photonic angular momentum with structured light: a review," Adv. Photonics **3**, 064001 (2021).
12. M. Padgett and R. Bowman, "Tweezers with a twist," Nat. Photonics **5**, 343–348 (2011).
13. Z. Shen, Z. J. Hu, G. H. Yuan, C. J. Min, H. Fang, and X.-C. Yuan, "Visualizing orbital angular momentum of plasmonic vortices," Opt. Lett. **37**, 4627–4629 (2012).
14. L. P. Gong, B. Gu, G. H. Rui, Y. P. Cui, Z. Q. Zhu, and Q. W. Zhan, "Optical forces of focused femtosecond laser pulses on nonlinear optical Rayleigh particles," Photonics Res. **6**, 138–143 (2018).
15. A. Nicolas, L. Veissier, L. Giner, E. Giacobino, D. Maxein, and J. Laurat, "A quantum memory for orbital angular momentum photonic qubits," Nat. Photonics **8**, 234–238 (2014).
16. D.-S. Ding, W. Zhang, Z.-Y. Zhou, S. Shi, G.-Y. Xiang, X.-S. Wang, Y.-K. Jiang, B.-S. Shi, and G.-C. Guo, "Quantum storage of orbital angular momentum entanglement in an atomic ensemble," Phys. Rev. Lett. **114**, 050502 (2015).
17. M. Erhard, R. Fickler, M. Krenn, and A. Zeilinger, "Twisted photons: new quantum perspectives in high dimensions," Light Sci. Appl. **7**, 17146 (2018).
18. F. Q. Kong, C. M. Zhang, F. Bouchard, Z. Y. Li, G. G. Brown, D. H. Ko, T. J. Hammond, L. Arissian, R. W. Boyd, E. Karimi, and P. B. Corkum, "Controlling the orbital angular momentum of high harmonic vortices," Nat. Commun. **8**, 14970 (2017).
19. D. Gauthier, P. R. Ribič, G. Adhikary, A. Camper, C. Chappuis, R. Cucini, L. F. DiMauro, G. Dovillaire, F. Frassetto, R. Géneaux, P. Miotti, L. Poletto, B. Ressel, C. Spezzani, M. Stupar, T. Ruchon, and G. De Ninno, "Tunable orbital angular momentum in high-harmonic generation," Nat. Commun. **8**, 14971 (2017).
20. G. Musarra, K. E. Wilson, D. Faccio, and E. M. Wright, "Rotation-dependent nonlinear absorption of orbital angular momentum beams in ruby," Opt. Lett. **43**, 3073–3075 (2018).
21. P. Chen, L.-L. Ma, W. Duan, J. Chen, S.-J. Ge, Z.-H. Zhu, M.-J. Tang, R. Xu, W. Gao, T. Li, W. Hu, and Y.-Q. Lu, "Digitalizing self-assembled chiral superstructures for optical vortex processing," Adv. Mater. **30**, 1705865 (2018).
22. S. Syubaev, A. Zhizhchenko, A. Kuchmizhak, A. Porfirev, E. Pustovalov, O. Vitrik, Y. Kulchin, S. Khonina, and S. Kudryashov, "Direct laser printing of chiral plasmonic nanojets by vortex beams," Opt. Express **25**, 10214–10223 (2017).
23. F. Takahashi, K. Miyamoto, H. Hidai, K. Yamane, R. Morita, and T. Omatsu, "Picosecond optical vortex pulse illumination forms a monocrystalline silicon needle," Sci. Rep. **6**, 21738 (2016).
24. P. S. Tan, X.-C. Yuan, G. H. Yuan, and Q. Wang, "High-resolution wide-field standing-wave surface plasmon resonance fluorescence microscopy with optical vortices," Appl. Phys. Lett. **97**, 241109 (2010).
25. C. L. Zhang, C. J. Min, L. P. Du, and X.-C. Yuan, "Perfect optical vortex enhanced surface plasmon excitation for plasmonic structured illumination microscopy imaging," Appl. Phys. Lett. **108**, 201601 (2016).
26. S. B. Wei, T. Lei, L. P. Du, C. L. Zhang, H. K. Chen, Y. Yang, S. W. Zhu, and X.-C. Yuan, "Sub-100 nm resolution PSIM by utilizing modified optical vortices with fractional topological charges for precise phase shifting," Opt. Express **23**, 30143–30148 (2015).
27. G. D. M. Jeffries, J. S. Edgar, Y. Q. Zhao, J. P. Shelby, C. Fong, and D. T. Chiu, "Using polarization-shaped optical vortex traps for single-cell nanosurgery," Nano Lett. **7**, 415–420 (2007).
28. W. Brullot, M. K. Vanbel, T. Swusten, and T. Verbiest, "Resolving enantiomers using the optical angular momentum of twisted light," Sci. Adv. **2**, e1501349 (2016).

29. Y. Zhao, A. N. Askarpour, L. Y. Sun, J. W. Shi, X. Q. Li, and A. Alù, "Chirality detection of enantiomers using twisted optical metamaterials," Nat. Commun. **8**, 14180 (2017).

30. G. A. Swartzlander, Jr., E. L. Ford, R. S. Abdul-Malik, L. M. Close, M. A. Peters, D. M. Palacios, and D. W. Wilson, "Astronomical demonstration of an optical vortex coronagraph," Opt. Express **16**, 10200–10207 (2008).

31. A. Aleksanyan, N. Kravets, and E. Brasselet, "Multiple-star system adaptive vortex coronagraphy using a liquid crystal light valve," Phys. Rev. Lett. **118**, 203902 (2017).

32. A. Aleksanyan and E. Brasselet, "High-charge and multiple-star vortex coronagraphy from stacked vector vortex phase masks," Opt. Lett. **43**, 383–386 (2018).

33. Y. Ma, B. Y. Wei, L. Y. Shi, A. K. Srivastava, V. G. Chigrinov, H.-S. Kwok, W. Hu, and Y. Q. Lu, "Fork gratings based on ferroelectric liquid crystals," Opt. Express **24**, 5822–5828 (2016).

34. B.-Y. Wei, W. Hu, Y. Ming, F. Xu, S. Rubin, J.-G. Wang, V. Chigrinov, and Y.-Q. Lu, "Generating switchable and reconfigurable optical vortices via photopatterning of liquid crystals," Adv. Mater. **26**, 1590–1595 (2014).

35. X. Y. Hu, Q. Zhao, P. P. Yu, X. L. Li, Z. Q. Wang, Y. M. Li, and L. Gong, "Dynamic shaping of orbital-angular-momentum beams for information encoding," Opt. Express **26**, 1796–1808 (2018).

36. C. H. Kai, Z. K. Feng, M. I. Dedo, P. Huang, K. Guo, F. Shen, J. Gao, and Z. Y. Guo, "The performances of different OAM encoding systems," Opt. Commun. **430**, 151–157 (2018).

37. E. Karimi, B. Piccirillo, E. Nagali, L. Marrucci, and E. Santamato, "Efficient generation and sorting of orbital angular momentum eigenmodes of light by thermally tuned q-plates," Appl. Phys. Lett. **94**, 231124 (2009).

38. W. Ji, C.-H. Lee, P. Chen, W. Hu, Y. Ming, L. J. Zhang, T.-H. Lin, V. Chigrinov, and Y.-Q. Lu, "Meta-q-plate for complex beam shaping," Sci. Rep. **6**, 25528 (2016).

39. S. Slussarenko, A. Murauski, T. Du, V. Chigrinov, L. Marrucci, and E. Santamato, "Tunable liquid crystal q-plates with arbitrary topological charge," Opt. Express **19**, 4085–4090 (2011).

40. W. H. Zhang, Q. Q. Qi, J. Zhou, and L. X. Chen, "Mimicking Faraday rotation to sort the orbital angular momentum of light," Phys. Rev. Lett. **112**, 153601 (2014).

41. G. C. G. Berkhout, M. P. J. Lavery, J. Courtial, M. W. Beijersbergen, and M. J. Padgett, "Efficient sorting of orbital angular momentum states of light," Phys. Rev. Lett. **105**, 153601 (2010).

42. M. Mirhosseini, M. Malik, Z. M. Shi, and R. W. Boyd, "Efficient separation of the orbital angular momentum eigenstates of light," Nat. Commun. **4**, 2781 (2013).

43. Y. H. Wen, I. Chremmos, Y. J. Chen, J. B. Zhu, Y. F. Zhang, and S. Y. Yu, "Spiral transformation for high-resolution and efficient sorting of optical vortex modes," Phys. Rev. Lett. **120**, 193904 (2018).

44. A. Overvig and A. Alù, "Wavefront-selective Fano resonant metasurfaces," Adv. Photonics **3**, 026002 (2021).

45. J. Yao, R. Lin, M. K. Chen, and D. P. Tsai, "Integrated-resonant metadevices: a review," Adv. Photonics **5**, 024001 (2023).

46. S. T. Mei, K. Huang, H. Liu, F. Qin, M. Q. Mehmood, Z. J. Xu, M. H. Hong, D. H. Zhang, J. H. Teng, A. Danner, and C.-W. Qiu, "On-chip discrimination of orbital angular momentum of light with plasmonic nanoslits," Nanoscale **8**, 2227–2233 (2016).

47. J. Chen, X. Chen, T. Li, and S. N. Zhu, "On-chip detection of orbital angular momentum beam by plasmonic nanogratings," Laser Photonics Rev. **12**, 1700331 (2018).

48. F. Feng, G. Y. Si, C. J. Min, X. C. Yuan, and M. Somekh, "On-chip plasmonic spin-Hall nanograting for simultaneously detecting phase and polarization singularities," Light Sci. Appl. **9**, 95 (2020).

49. X. S. Zhao, X. Feng, F. Liu, K. Y. Cui, W. Zhang, and Y. D. Huang, "A compound phase-modulated beam splitter to distinguish both spin and orbital angular momentum," ACS Photonics **7**, 212–220 (2020).

50. F. Feng, S.-B. Wei, L. Li, C.-J. Min, X.-C. Yuan, and M. Somekh, "Spin-orbit coupling controlled near-field propagation and focusing of Bloch surface wave," Opt. Express **27**, 27536–27545 (2019).

51. W. J. Kong, Z. Zheng, Y. H. Wan, S. N. Li, and J. S. Liu, "High-sensitivity sensing based on intensity-interrogated Bloch surface wave sensors," Sens. Actuators B Chem. **193**, 467–471 (2014).

52. M. U. Khan and B. Corbett, "Bloch surface wave structures for high sensitivity detection and compact waveguiding," Sci. Technol. Adv. Mater. **17**, 398–409 (2016).

53. A. L. Lereu, M. Zerrad, A. Passian, and C. Amra, "Surface plasmons and Bloch surface waves: Towards optimized ultra-sensitive optical sensors," Appl. Phys. Lett. **111**, 011107 (2017).

54. Y. Kuai, Z. B. Xie, J. X. Chen, H. Q. Gui, L. Xu, C. F. Kuang, P. Wang, X. Liu, J. G. Liu, J. R. Lakowicz, and D. G. Zhang, "Real-time measurement of the hygroscopic growth dynamics of single aerosol nanoparticles with Bloch surface wave microscopy," ACS Nano **14**, 9136–9144 (2020).

55. Y. Kuai, J. X. Chen, Z. T. Fan, G. Zou, J. R. Lakowicz, and D. G. Zhang, "Planar photonic chips with tailored angular transmission for high-contrast-imaging devices," Nat. Commun. **12**, 6835 (2021).

56. Y. F. Xiang, X. Tang, Y. N. Fu, F. Y. Lu, Y. Kuai, C. J. Min, J. X. Chen, P. Wang, J. R. Lakowicz, X. C. Yuan, and D. G. Zhang, "Trapping metallic particles using focused Bloch surface waves," Nanoscale **12**, 1688–1696 (2020).

57. R. X. Wang, Y. Wang, D. G. Zhang, G. Y. Si, L. F. Zhu, L. P. Du, S. S. Kou, R. Badugu, M. Rosenfeld, J. Lin, P. Wang, H. Ming, X. C. Yuan, and J. R. Lakowicz, "Diffraction-free Bloch surface waves," ACS Nano **11**, 5383–5390 (2017).

58. D. G. Zhang, R. X. Wang, Y. F. Xiang, Y. Kuai, C. F. Kuang, R. Badugu, Y. K. Xu, P. Wang, H. Ming, X. Liu, and J. R. Lakowicz, "Silver nanowires for reconfigurable Bloch surface waves," ACS Nano **11**, 10446–10451 (2017).

59. D. G. Zhang, Y. F. Xiang, J. X. Chen, J. J. Cheng, L. F. Zhu, R. X. Wang, G. Zou, P. Wang, H. Ming, M. Rosenfeld, R. Badugu, and J. R. Lakowicz, "Extending the propagation distance of a silver nanowire plasmonic waveguide with a dielectric multilayer substrate," Nano Lett. **18**, 1152–1158 (2018).

60. J. Lin, J. P. B. Mueller, Q. Wang, G. H. Yuan, N. Antoniou, X.-C. Yuan, and F. Capasso, "Polarization-controlled tunable directional coupling of surface plasmon polaritons," Science **340**, 331–334 (2013).

61. L. Quintino, A. Costa, R. Miranda, D. Yapp, V. Kumar, and C. J. Kong, "Welding with high power fiber lasers a preliminary study," Mater. Des. **28**, 1231–1237 (2007).

62. L. Novotny, "Effective wavelength scaling for optical antennas," Phys. Rev. Lett. **98**, 266802 (2007).

63. R.-H. Jiang, C. Chen, D.-Z. Lin, H.-C. Chou, J.-Y. Chu, and T.-J. Yen, "Near-field plasmonic probe with super resolution and high throughput and signal-to-noise ratio," Nano Lett. **18**, 881–885 (2018).

64. Y. Z. Sun, X. H. Yan, S. Blaize, R. Bachelot, H. Wei, and W. Ding, "Phase-resolved all-fiber reflection-based s-NSOM for on-chip characterization," Opt. Express **30**, 41118–41132 (2022).

65. P. Shi, A. P. Yang, F. F. Meng, J. S. Chen, Y. Q. Zhang, Z. W. Xie, L. P. Du, and X. C. Yuan, "Optical near-field measurement for spin-orbit interaction of light," Prog. Quantum Electron. **78**, 100341 (2021).

66. A. L. Lereu, A. Passian, and P. Dumas, "Near field optical microscopy: a brief review," Int. J. Nanotechnol. **9**, 488–501 (2012).

67. B. Hecht, B. Sick, U. P. Wild, V. Deckert, R. Zenobi, O. J. F. Martin, and D. W. Pohl, "Scanning near-field optical microscopy with aperture probes: fundamentals and applications," J. Chem. Phys. **112**, 7761–7774 (2000).

68. J. R. Zhang, Z. Y. Guo, K. Y. Zhou, L. L. Ran, L. Zhu, W. Wang, Y. X. Sun, F. Shen, J. Gao, and S. T. Liu, "Circular polarization analyzer based on an Archimedean nano-pinholes array," Opt. Express **23**, 30523–30531 (2015).

69. Q. Zhang, P. Y. Li, Y. Y. Li, X. R. Ren, and S. Y. Teng, "A universal plasmonic polarization state analyzer," Plasmonics **13**, 1129–1134 (2018).